Supplementary Materials for

Nano-optic endoscope for high-resolution optical coherence tomography *in vivo*

Hamid Pahlevaninezhad[1,2] †, Mohammadreza Khorasaninejad[2] †, Yao-Wei Huang[2,3] †, Zhujun Shi[4], Lida P. Hariri[1], David C. Adams[1], Vivien Ding[2,5], Alexander Zhu[2], Cheng-Wei Qiu[3], Federico Capasso[2*], and Melissa J. Suter[1*]

[1]*Harvard Medical School and Massachusetts General Hospital, Boston MA 02114, United States*

[2]*John A. Paulson School of Engineering and Applied Science, Harvard University, Cambridge MA 02138, United States*

[3]*Department of Electrical and Computer Engineering, National University of Singapore, 117583 Singapore, Singapore*

[4]*Department of Physics, Harvard University, Cambridge, MA 02138, United States*

[4]*Department of Electrical and Computer Engineering, University of Waterloo, Waterloo Ontario N2L 3G1, Canada*

†: These authors contributed equally to this work.

*Corresponding author email: capasso@seas.harvard.edu, msuter@mgh.harvard.edu

I. Metalens phase profile calculation

We use ray tracing to calculate source-to-lens (L_{sl}) and lens-to-focal point (L_{lf}) optical path lengths in the nano-optic endoscope shown in Figure S1a. Given the geometry of the structure and the coordinates defined in Figure S1a,

$$L_{sl} = n_{sheath}\sqrt{\left(x'-x'_s\right)^2 + \left(y'-y'_s\right)^2 + z'^2_s} \quad (1)$$

where $(x', y', 0)$ and (x_s', y_s', z_s') are the metalens and source (fiber facet center) coordinates. To calculate L_{lf}, a focal point with fixed coordinates is assumed at P_0 to be the intersection of rays with θ_0 and δ_0 inclinations with respect to $x'z'$- and $y'z'$-planes (Figure 1Sb). The optical path length of each ray is calculated by tracing its optical path from the focal point to the metalens ($\overline{P_0P_1P_2P_3}$) as follows. A pair of inclination angles (θ_0, δ_0) defines a line passing through P_0 along the direction $\hat{v}_1 = [\sin\theta_0\sin\delta_0, \sin\theta_0\cos\delta_0, \cos\theta_0]$. The intersection of this line with the sheath outer surface expressed as

$$f(x', y', x') = x'^2 + \left[(z' - T)\cos\beta - y'\sin\beta\right]^2 = R_{\max}^2 \qquad (2)$$

($R_{\max}$ is the sheath outer radius and T is the sheath axis offset with respect to the origin in z'-direction) yields P_1 coordinates and, in turn, $\overline{P_0P_1}$ path length. P_1 coordinates and Snell's law determine the light path in the sheath along the direction $\hat{v}_2 = \sin\gamma_2\ \hat{u}_1 + \cos\gamma_2\ \hat{n}_1$ where $\hat{n}_1$ (= $\nabla f / |\nabla f|$) is the unit vector normal to the sheath outer surface at P_1, $\gamma_2 = \sin^{-1}(\sin\gamma_1 / n_{glass})$, $\gamma_1 = \cos^{-1}(\hat{v}_1 .\ \hat{n}_1)$, and $\hat{u}_1 = \hat{n}_1 \times (\hat{v}_1 \times \hat{n}_1)$. P_2, P_3 and the corresponding optical path lengths are determined in a similar way. Varying (θ_0, δ_0), we obtain the optical path lengths corresponding to rays from different positions on the metalens to the focal spot. Figure S1c shows the phase profile that metalens needs to impart to null optical path length differences between rays. We validate this approach analytically and with numerical simulations. The former uses the generalized Snell's law[33], explicitly $\vec{k}_{t,\|} = \vec{k}_{i,\|} + \nabla\varphi$, to account for the additional momentum induced by the metalens phase gradient ($\nabla\varphi$) to the components of incident beam momentum parallel to the surface ($\vec{k}_{i,\|}$), resulting in a change in the same component of the transmitted beam momentum ($\vec{k}_{t,\|}$) and, in turn, a change in the refraction angle. The latter uses a commercial ray tracing software (OpticStudio, Zemax LLC) to simulate the endoscope distal end optics. Both confirm that all rays converge to a point at P_0 within the Airy disc (Figure S1d).

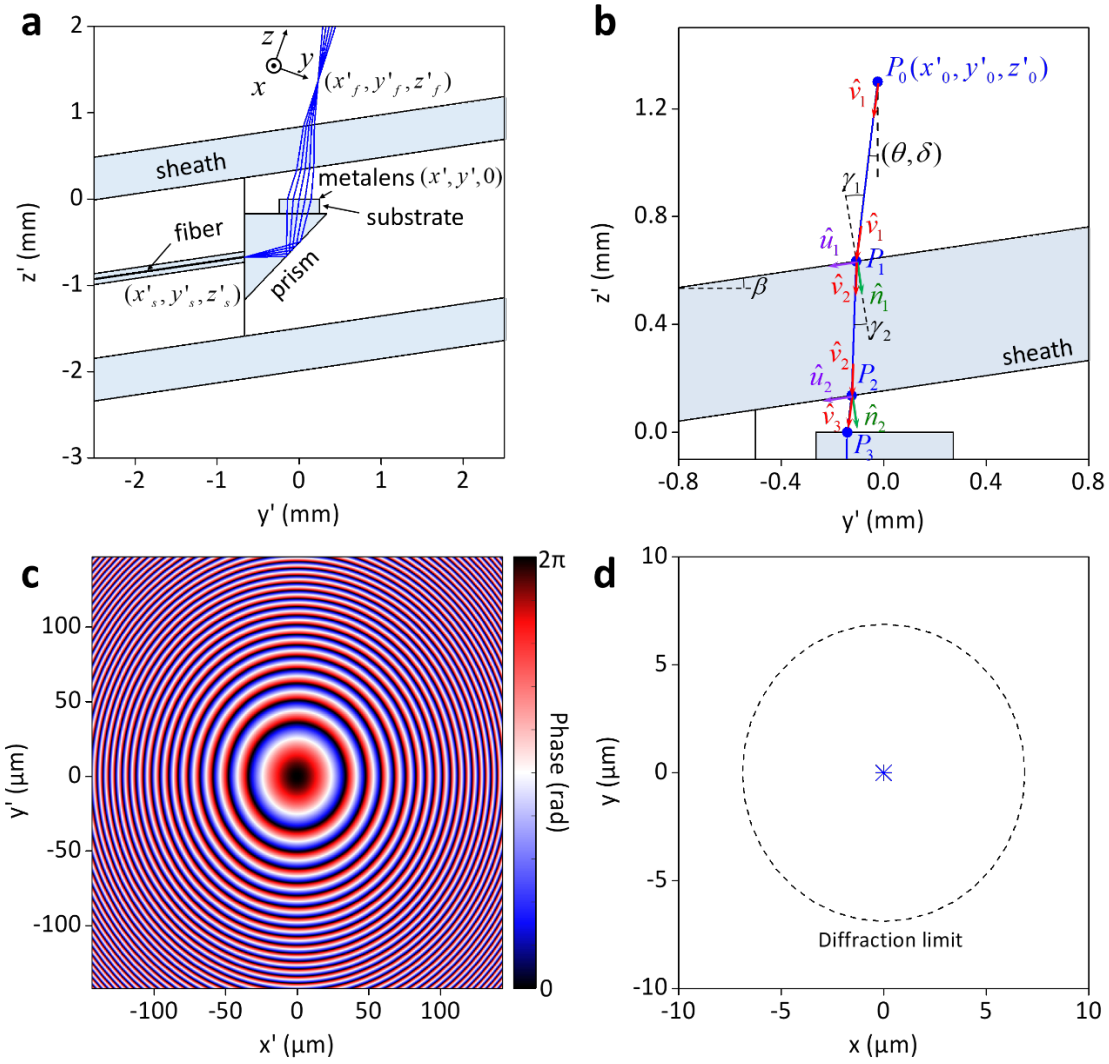

Figure S1. Metalens design using ray-tracing. a, Side view of the nano-optic endoscope and ray-tracing (blue lines). The origin of (x', y', z') coordinates is at the metalens center. **b**, Schematic illustrating a ray trajectory from the focal point to a point on the metalens. **c**, Metalens phase profile based on the analytical calculations. **d**, Validation of calculated phase with ray-tracing. The blue symbol indicates the intersections of rays from the metalens to the focal plane. The dashed line corresponds to the first minimum of Airy disc. Calculations are at the center wavelength, 1310 nm.

II. Nanopillars computational analysis

The amorphous silicon (a-Si) nanopillars, the building blocks of the metalens, are characterized in terms of cumulative phase delay and power transmittance in the wavelength range of interest using a commercial finite difference time domain (FDTD) solver (Lumerical Inc., Vancouver). Given the geometry of the nano-optic endoscope distal end, the optical field incident on nanopillars is slightly tilted (8˚for the chief ray) with respect to the nanopillars' axes. As a result, the metalens is not strictly polarization-independent. To assess the degree of polarization dependence, we perform the computational analyses for both transverse electric (TE) and transverse magnetic (TM) modes using Bloch boundaries. Results, summarized in Figure S2, include transmittance and phase delays of the nanopillars with different diameters for both modes in the 1200 to 1400 nm wavelength range. Nanopillars with correct diameters to impart the required phase delays are selected to compose the metalens. Comparison of the results for the two modes indicates negligible polarization dependence. All nanopillars selected for the metalens in our design have higher than 80% transmittance and impart phase delays spanning 0 to 2π.

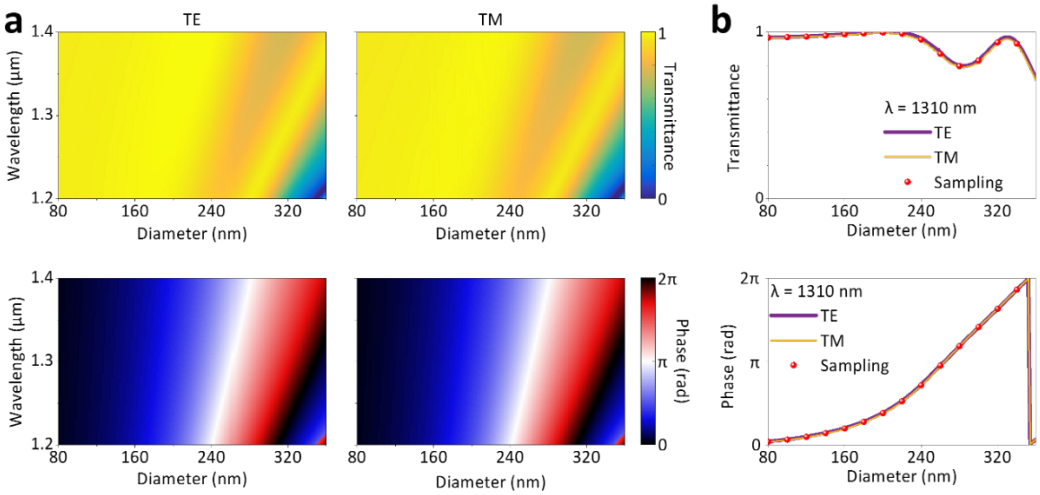

Figure S2. Computational analysis of a-Si nanopillars. a, Nanopillars transmittance and phase delays with respect to the diameter in the wavelength range of interest for TE and TM modes calculated by an FDTD solver. **b**, Graphs of the results at the design wavelength 1310 nm. Red circles indicate the selected nanopillars in our design. Polarization dependence is small.

III. Nano-optic endoscope wave analysis

Accurate analysis of the nano-optic endoscope output beam requires full-wave analysis using numerical techniques such as FDTD. However, these techniques are computationally intensive and impractical for the large structures we intend to model. Therefore, we use a Fresnel-Kirchhoff integral to obtain the optical field at the output of the nano-optic endoscope as follows. A Gaussian beam with a 9.2 μm mode-field-diameter is assumed as a light source modeling the light at the fiber end facet. The phase and amplitude of the field incident on the metalens are then calculated. Accounting for the transmittance and phase delays of nanopillars for both TE and TM modes, the intensity at the specific point outside of the endoscope is obtained by integrating all fields from the nanopillars given the optical paths calculated based on the ray-tracing (Section I in the Supplementary materials).

Figure S3 illustrates the results including beam profiles in the tangential, sagittal, and focal planes at five wavelengths from 1250 to 1370 nm. Symmetric focal spot profiles are observed with full widths at half maximum spanning from 7.9 to 9.6 μm across the wavelength range. Higher numerical apertures at longer wavelengths give rise to a reduced focal spot size. A wavelength variation from 1250 to 1370 nm causes a 303 μm axial shift in the focal point. Identical beam profiles in the tangential and sagittal planes signifies no appreciable astigmatism.

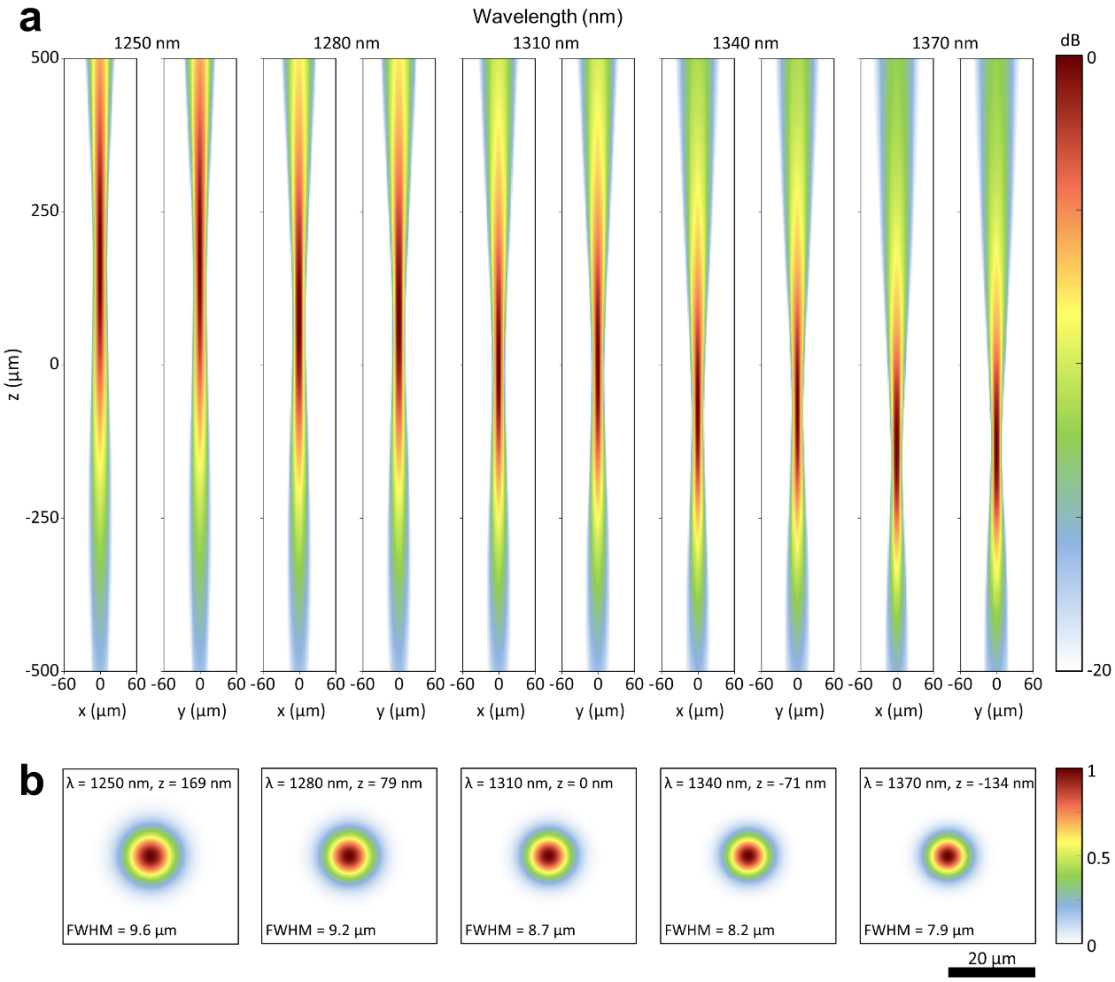

Figure S3. Wave analysis of nano-optic endoscope. a, Calculated tangential (*yz*-plane) and sagittal (*xz*-plane) intensity distributions of the nano-optic endoscope output beam at five wavelengths from 1250 to 1370 nm. **b**, Spot profiles of the focal planes at the five wavelengths.

IV. Nano-optic endoscope characterization

To experimentally assess the nano-optic endoscope output beam we use a custom-built setup shown schematically in Figure S4. The nano-optic endoscope is optically pumped by a supercontinuum laser (SuperK Extreme, NKT Photonics). Images of the output beam are

captured at different axial points using an infinity-corrected objective (Mitutoyo Plan Apo NIR HR, 50×, NA = 0.65) paired with a tube lens (f = 180 mm) and an InGaAs camera (Raptor OWL 640 Analog VIS-SWIR). 3-dimentional beam profiles are measured for different wavelengths by scanning the objective lens in the axial direction, creating images with 0.3 by 0.3 µm lateral and 10 µm axial resolution.

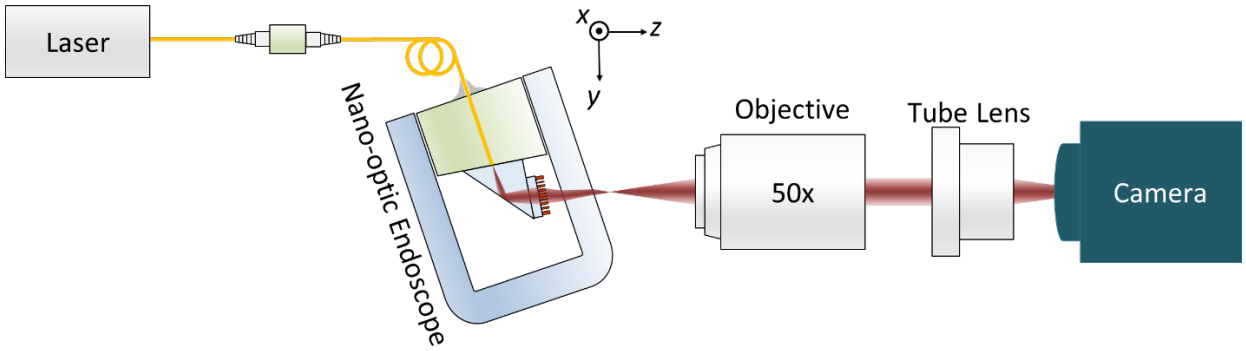

Figure S4. Measurement setup used for output beam characterization. The endoscope is pumped by a fiber-coupled supercontinuum laser at individual wavelengths in the range of interest. A combination of an objective (NA = 0.65), a tube lens (f = 180 mm), and an infrared camera is used to image the catheter output beam.

Figure 3 and Figure S5 show the results of the measurements for the nano-optic endoscope along with those for a commercial GRIN lens catheter and a ball lens catheter (measured using the setup described above). In contrast to the focal spots of the nano-optic endoscope, significant astigmatism is observed for the GRIN lens catheter and the ball lens catheter. Figure S6a shows very similar intensity beam at the tangential and sagittal planes with approximately 22 µm focal point differences in the two planes, further confirming the small astigmatism of the nano-optic endoscope. A wavelength variation from 1250 to 1370 nm results

in a 285 µm axial shift in the focal point and 12.7 to 7.4 µm change in the focal spot full-width at half-maximum (Figure 6Sb).

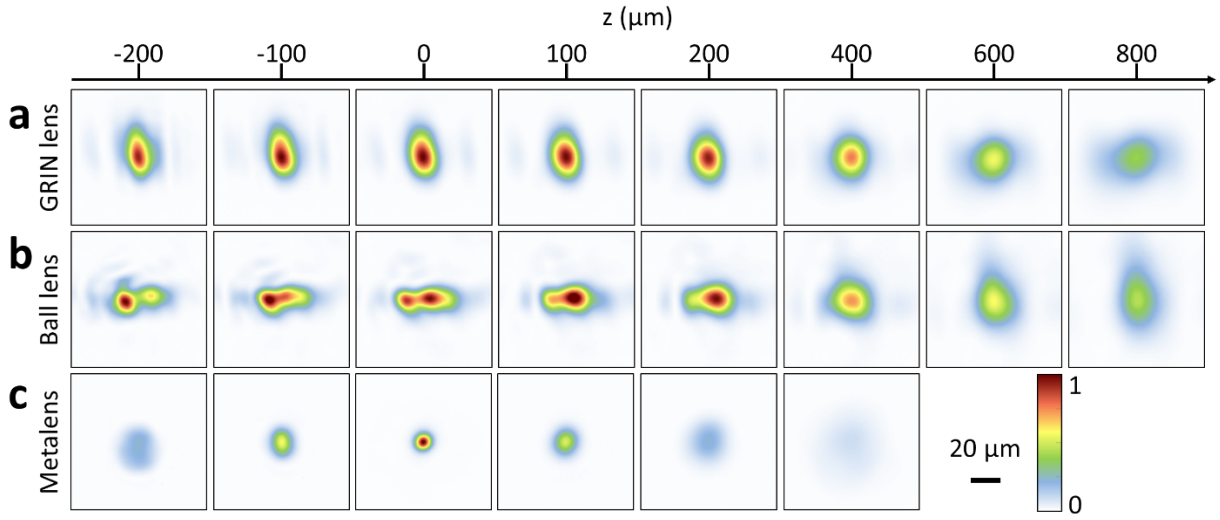

Figure S5. Comparison of the nano-optic endoscope beam profile with those of a GRIN lens catheter and a ball lens catheter. Lateral sections of the optical output beams of a GRIN lens catheter (**a**), a ball lens catheter (**b**), and the nano-optic endoscope (**c**) at different axial points (*z*). Significantly tighter, near aberration-free focal spot profile is observed for the nano-optic endoscope in contrast to the astigmatic profiles of the GRIN lens catheter and the ball lens catheter. All measurements are at 1310 nm wavelength and the axial coordinate is relative to the focal point for each catheter.

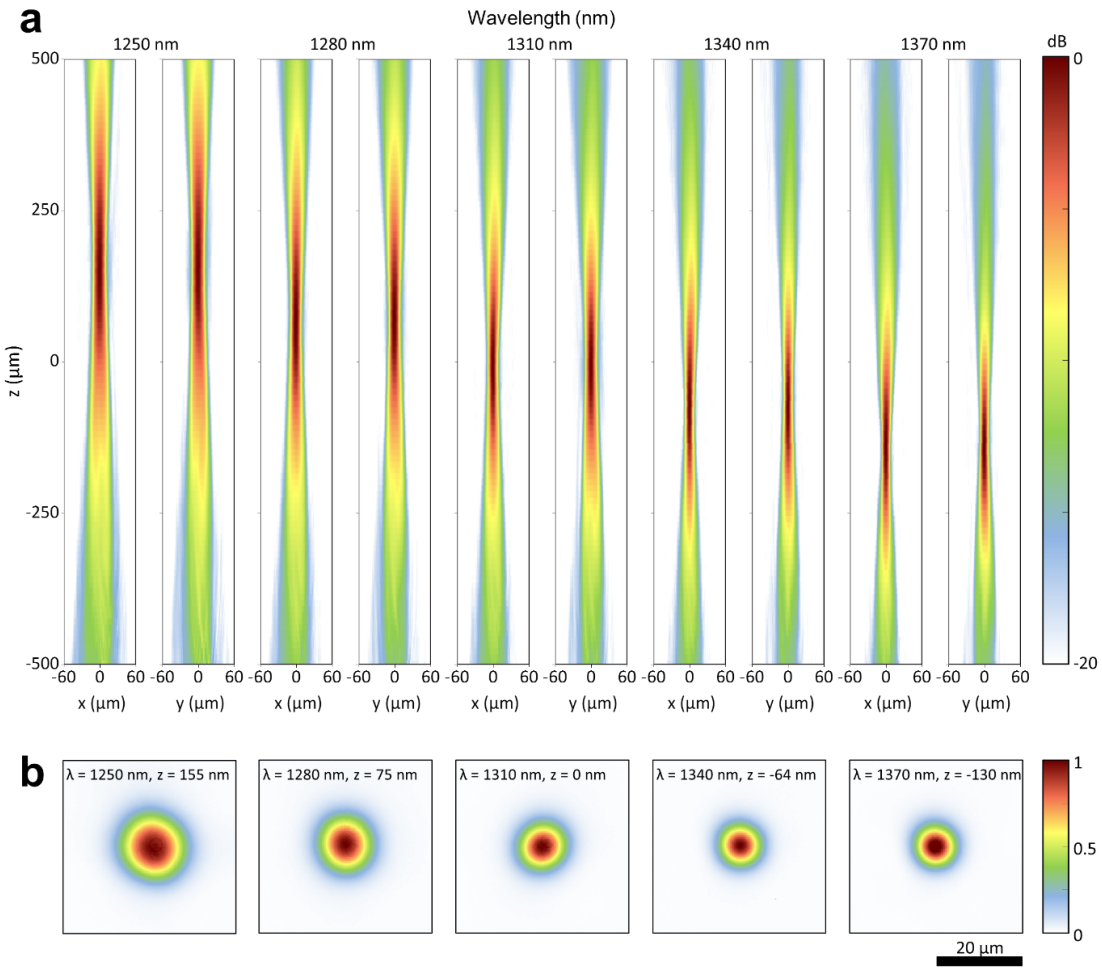

Figure S6. Measured beam profile of the nano-optic endoscope. a, Nano-optic endoscope output beam intensity distributions measured in the tangential and sagittal planes. **b**, Focal spots at different wavelengths. Near symmetric focal spot profiles are observed at five wavelengths spanning the wavelength range of interest.

Figure S7 compares the measured properties of the nano-optic endoscope output beam with calculations and the diffraction limit. We used a Fresnel-Kirchhoff integral to calculate the theoretical spot size as assumptions of Abbe's diffraction limit do not hold; Abbe's diffraction

limit is the result of coherent superposition of two Airy diffraction patterns at the image plane that implicitly assume uniform distribution of beam incident on the lens. However, this is not the case for the nano-optic endoscope as the optical beam emanating from the single mode fiber is Gaussian and, as a result, the incident beam on the metalens is also Gaussian (not plane wave). Therefore, accurate estimation of the expected values entails calculation of a Fresnel-Kirchhoff integral that accounts for the spatial amplitude variations (Section III). Figure S7 confirms that the measured results are in excellent agreement with the theoretical expectations across most of the wavelength range (some deviations were observed at the lower limit). Results validate near diffraction-limited focusing.

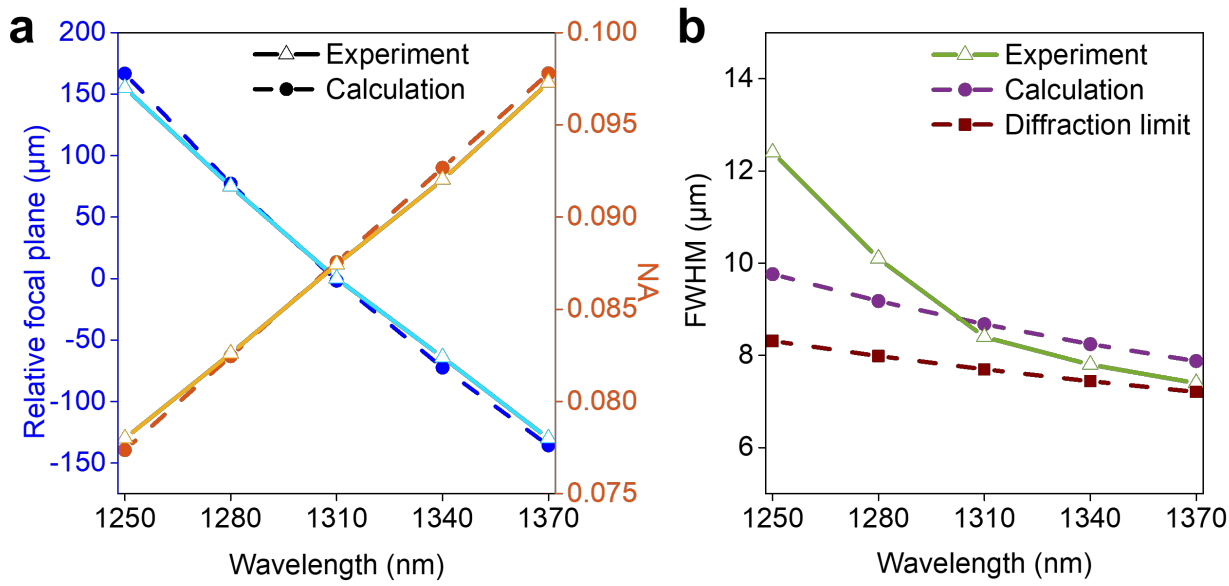

Figure S7. Comparison of measured beam properties of the nano-optic endoscope with theoretical limits. a, Comparison of measured relative focal plane and numerical aperture (NA) of the nano-optic endoscope with values obtained from the Fresnel-Kirchhoff integral analysis. **b**, Comparison of measured

FWHM of the nano-optic endoscope with values obtained from the Fresnel-Kirchhoff integral analysis and Abbe's diffraction limits.

The insertion loss of the fabricated nano-optic endoscope is measured to be slightly higher (0.75 dB, averaged over the wavelength range) than that of the GRIN lens and ball lens catheters. The existence of more interfaces in the distal end of the nano-optic endoscope in combination with the deviation of the metalens transmissivity from unity are likely responsible for this increased loss. However, such small losses do not impact the image quality as the state-of-the-art OCT systems can readily reach sensitivities higher than 100 dB.

V. Analytic approach to spectral interferometry with a chromatic lens

To assess the effects of the metalens chromatic dispersion on spectral interferometry we assume a Gaussian beam illumination propagating in the z-direction with a waist location that varies axially with the wavenumber expressed mathematically as

$$E_i = A_i \frac{w_0}{w} e^{-\frac{x^2+y^2}{w^2}} e^{ik_i z - \omega t} \tag{3}$$

$$w = w_0 \sqrt{1 + \left(\frac{z - z_0}{z_R} \right)^2} \tag{4}$$

$$z_0 = m\left(k_i - k_0\right) + f_0 \tag{5}$$

$$z_R = k_i w_0^2 / 2 \tag{6}$$

to model the metalens output beam, where Equation (5) represents the focal point deviations from f_0, the focal point at the center wavenumber (k_0), with respect to the wavenumber (k_i) and z_R

is the Rayleigh range (field curvature is neglected, a valid approximation if numerical aperture is not large). Following Fercher's treatment[40], the first Born approximation gives the scattered field

$$E_s = -\frac{1}{4\pi}\int_{V(\boldsymbol{r}')} F(\boldsymbol{r}')E_i(\boldsymbol{r}', \boldsymbol{k}_i)\frac{e^{i\boldsymbol{k}_s\cdot(\boldsymbol{r}-\boldsymbol{r}')}}{|\boldsymbol{r}-\boldsymbol{r}'|}d^3\boldsymbol{r}' \qquad (7)$$

where F is the scattering potential to be determined, $V(\boldsymbol{r}')$ is the illuminated scattering volume, $\boldsymbol{k}_s$ is the scattered wavevector, and $\boldsymbol{r}$ and $\boldsymbol{r}'$ are, respectively, input beam and scatterer coordinates. Assuming the scattering volume depth is small compared to its distance from the measurement point ($|\boldsymbol{r} - \boldsymbol{r}'| \approx D$: measurement distance from the scattering volume surface) and only elastically scattered fields are detected ($\boldsymbol{k}_i = -\boldsymbol{k}_s = \boldsymbol{k}$), the scattered field is simplified to

$$E_s = -\frac{A_i w_0}{4\pi D}e^{ikz-i\omega t}\int_V F(x', y', z')\frac{e^{-\frac{(x'-x)^2+(y'-y)^2}{w^2}}}{w}e^{-i2kz'}dx'dy'dz'. \qquad (8)$$

Equation (8) represents the scattered field from tissue in the sample arm. Similarly, the reflected beam from the mirror in the reference arm (E_s^{ref}) can be obtained by inserting $F \approx F_0^{ref}\,\delta(z' - z_{\mathrm{ref}})$ in Equation (8) that gives

$$E_s^{ref} = A_{ref}e^{ikz-i\omega t}e^{-i2kz_{ref}}. \qquad (9)$$

The signal measured by the photodetectors is proportional to the product of the sample field and the complex conjugate of the reference field and can be expressed as

$$I(k) \propto \int_V F(x', y', z')\frac{e^{-\frac{(x'-x)^2+(y'-y)^2}{w^2}}}{w}e^{-i2k(z'-z_{ref})}dx'dy'dz'. \qquad (10)$$

In general, to reconstruct the scattering potential F with respect to the depth from $I(k)$ measurements, a Fredholm integral of first kind needs to be solved as explained later since the kernel is not strictly an oscillatory function. However, a Fourier transform (typically used for reconstruction of images in spectral interferometry) may still be a good approximation if the

complex exponential part of the kernel is the only part with fast variations with wavenumber. We use this approximation and determine the lateral point spread function using standard Fourier transform method as follows. A point scatterer at depth z_s expressed as $F = F_0\ \delta(x')\delta(y')\delta(z'-z_s)$ produces signal $I(k)$ proportional to

$$F_0 \frac{e^{-\frac{x^2+y^2}{w^2}}}{w} e^{i2k(z_{ref}-z_s)}. \tag{11}$$

The reconstructed tomogram from the Fourier transform of measurements in k-space is then

$$F(Z) = \int F_0 \frac{e^{-\frac{x^2+y^2}{w^2}}}{w} e^{i2k(Z-z_s)} dk\,, \tag{12}$$

where z_{ref} is assumed to be equal to the scattering volume depth reference without loss of generality.

To determine the expected lateral resolution of OCT system with the nano-optic endoscope, we calculate the integral in Equation (12) for a scatterer located at the depth point (z_s) accounting for three factors: 1) the focal point shift with the wavenumber according to the metalens chromatic dispersion, 2) the focal spot size variations with respect to the wavenumber due to the changes in NA, and 3) variations of our OCT swept-source amplitude with wavenumber (Figure S9). Then, F is averaged with respect to Z to obtain lateral point spread function of the OCT signal at the depth point numerically equal to z_s. Repeating the process for different z_s yields lateral point spread functions at different depth points of the scattering volume. Figure S8 shows the results including the lateral point spread function with respect to the depth for OCT signals obtained using the metalens and using an achromatic lens with the same NA (as that of metalens at the center wavelength). Compared to the case with the achromatic lens, significantly larger depth-of-focus is predicted for the metalens due to the axial focal point shift

with wavelength. Crucially, the ability to engineer the metalens chromatic dispersion provides opportunities to maintain high-resolution imaging far beyond the incident field Rayleigh range.

In general, reconstruction of tomograms from measurements in k-space for chromatic illumination requires solving a Fredholm integral of first kind. Because, inserting a laterally averaged scattering potential function $F(x', y', z') = F_{\text{avg}}(z')$ that varies only with depth into Equation (10) yields

$$I(k) = \int K(z', k) F(z') dz', \tag{13}$$

where

$$K(z', k) \propto w(z', k) e^{-i2k(z' - z_{ref})} \tag{14}$$

is the kernel. Equation (13) is a Fredholm integral of first kind that can be solved numerically using $I(k)$ measurements.

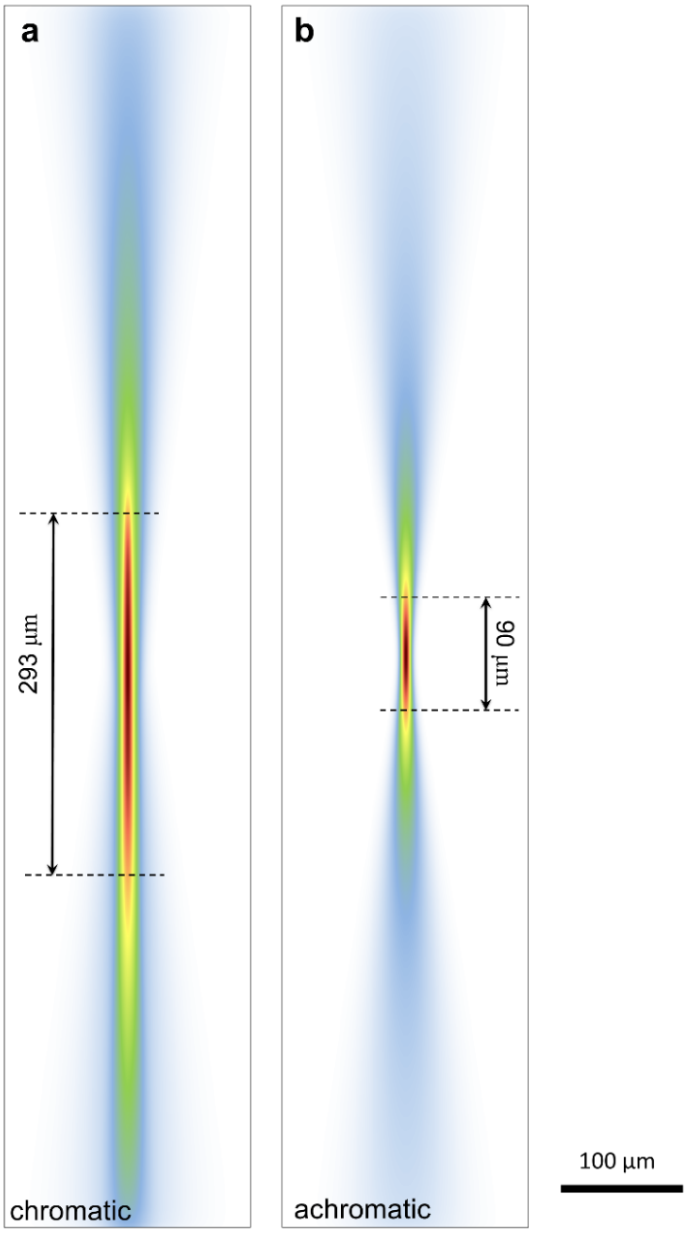

Figure S8. Analytic lateral point spread function of reconstructed signal from spectral interferometry. Lateral point spread function with respect to depth obtained from spectral interferometry analysis of single point scatterer at varying depth illuminated through a metalens (**a**) and through an achromatic lens with the same NA (**b**).

VI. OCT imaging system

All images are captured using a Fourier-domain OCT system built in house and shown schematically in Figure S9. The technical details of this system are previously reported[45]. Briefly, we use a wavelength-swept source consisting of a semiconductor optical amplifier (Covega Corp.) and a spinning polygon mirror (variable wavelength filter) sweeping the spectrum illustrated in Figure S9 at 68 kHz repetition rate. The interferometer includes a 90/10 fused fiber coupler that splits the field between the reference arm (10%) and the sample arm (90%). The reference arm contains a fixed reflector and an acousto-optic modulator (Brimrose Corp.) for shifting the interference signal away from DC. A fraction of the reference arm field is directed to a combination of a fiber Bragg grating (as a narrowband filter) and a fast photodetector to generate synchronizing trigger between wavelength sweeps. In the sample arm, a fiber optic rotary joint (FORJ) connects the nano-optic endoscope to the system. The field reflected from the reference mirror recombines with the signal backscattered from the sample in a polarization-diverse detection arm including a broadband beam splitter, two polarization beam splitters, and two balanced photodetectors (New Focus Corp.) for the detection of two orthogonal polarization components. The photodetectors' electrical output signals are digitized using a 14-bit dual channel 170MS/s data acquisition board (Signatec Inc.). 2248 samples are registered in each wavelength sweep (k-space) and sampled to 2048 8-bit depth pixels after the Fourier transform corresponding to 9.77 mm ranging depth (in air). With this configuration, the system achieve 33.2 frames/s imaging with 2048 A-lines/frame.

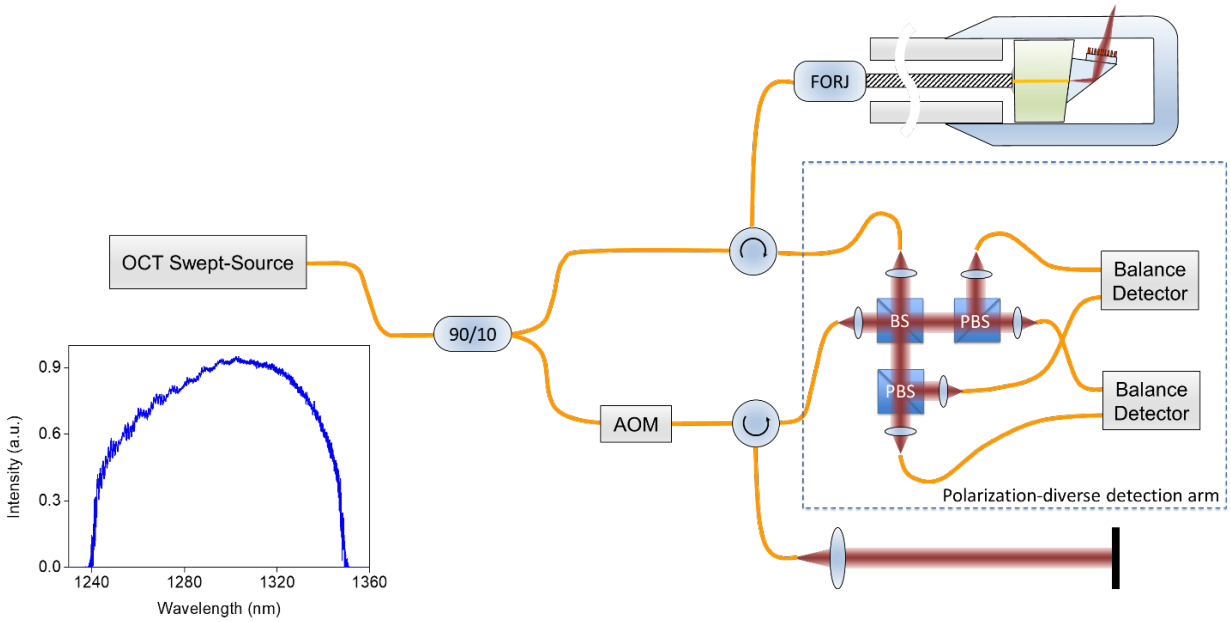

Figure S9. Endoscopic OCT system. Fourier-domain OCT system including a swept-source, a fiber-based Mach-Zehnder interferometer, sample and reference arms, and a polarization-diverse detection arm. Nano-optic endoscope is connected to the interferometer by a fiber optic rotary joint (FROJ) that provides rotational and translational motions of the endoscope distal optics. An acousto-optic optical modulator (AOM) removes depth degeneracy. The detection arm includes a broadband beam splitter (BS), two polarization beam splitters (PBS), and two balance detectors. The blue curve illustrates the spectrum swept by the source.